Jet Noise Measurements of an Installed GE F404 Engine

Kevin M. Leete[*], Aaron B. Vaughn[†], Michael S. Bassett[‡], Reese D. Rasband[§], Daniel J. Novakovich[¶] and Kent L. Gee[‖]
Brigham Young University, Provo, Utah, 84602

S. Conner Campbell [**]
Ball Aerospace, Fairborn, Ohio, 45324

Frank S. Mobley[††] and Alan T. Wall [‡‡]
Air Force Research Laboratory, Wright-Patterson AFB, Ohio, 45433

This paper describes noise measurements taken of the new Boeing T-7A Red Hawk trainer aircraft, which uses a single F404 afterburning turbofan engine. The extensive measurement satisfies the American National Standards Institute/Acoustical Society of America standard S12.75-2012 for ground run-up for future environmental impact assessment and includes additional locations around the aircraft to understand exposure by maintenance personnel. A large near-field array was also deployed to shed light on phenomena that are not generally seen in the measurement of laboratory-scale jets, such as the presence of spatiospectral lobes. Initial data analysis shows they are of high fidelity and contain similar phenomena as other recent high-performance jet aircraft noise measurements, including evidence of large and fine-scale noise radiation, broadband shock-associated noise, spatiospectral lobing at multiple engine powers, an upstream shifting of overall level directivity with engine power, and appreciable shock content in the measured waveforms. Further analysis of this dataset will add to the understanding of full-scale, high-speed jet noise and allow comparisons to similar numerical simulations and laboratory-scale measurements.

I. Nomenclature

MARP	=	Microphone array reference point
$\text{Sk}\{\partial p/\partial t\}$	=	Skewness of the time derivative of the pressure waveform, "derivative skewness"
$\text{Kurt}\{\partial p/\partial t\}$	=	Kurtosis of the time derivative of the pressure waveform, "derivative kurtosis"
x	=	Distance downstream of the nozzle exit
y	=	Distance from the jet centerline
z	=	Height above the ground

II. Introduction

The Air Force Research Laboratory (AFRL) led a multi-organizational effort to measure the noise generated by the new Boeing/Saab T-7A "Red Hawk" aircraft at Holloman Air Force Base in August 2019. The three purposes of the measurement were to a) characterize the noise for environmental and community impact assessment following the ANSI/ASA standard S12.75 for ground run-up, b) understand levels experienced by maintainers working around the aircraft during various operations, and c) increase understanding of the aeroacoustic noise sources generated by military aircraft, including phenomena not generally seen in laboratory-scale jet noise measurements.

---
[*]Graduate Student, Department of Physics and Astronomy, AIAA student member
[†]Graduate Student, Department of Physics and Astronomy, AIAA student member
[‡]Undergraduate Student, Department of Physics and Astronomy
[§]Graduate Student, Department of Physics and Astronomy
[¶]Undergraduate Student, Department of Physics and Astronomy
[‖]Professor of Physics, Department of Physics and Astronomy, AIAA member
[**]Engineer, 2875 Presidential Drive, Fairborn, OH,45324
[††]Research Physicist, Battlespace Acoustics Branch, 2610 Seventh St., Bldg. 441, Wright-Patterson AFB, OH 45433, AIAA Member.
[‡‡]Research Physicist, Battlespace Acoustics Branch, 2610 Seventh St., Bldg. 441, Wright-Patterson AFB, OH 45433, AIAA Member.

Numerous methods have been used to alter the jet flow produced by aircraft in an attempt to reduce the radiated noise [1]. Specifically for the F404 engine, the use of microjet injectors, [2], chevrons [3], contoured inserts [4] and twin jet nacelles [5] have been investigated for noise reduction. Of critical importance in developing these and future technologies is the understanding of how jet noise differs between full-scale installed engines, laboratory-scale models, and numerical simulations [6]. The addition of this dataset to growing repositories of measurements of high-performance aircraft will allow for further understanding of these complex noise mechanisms, which can inform future jet noise reduction studies.

In recent years, several measurements have been taken of full-scale military aircraft operating at various engine powers.[7–9] Subsequent analyses of these datasets show phenomena that are not often reproduced at laboratory scales, such as the presence of spatiospectral lobes [10]. Spatiospectral lobes are local maxima in the space-frequency domain, which manifests itself either as multiple peaks in a spectrum measured at a single location, or multiple maxima in the levels when plotting a single frequency across space. These spatiospectral lobes have been seen in measurements of aircraft with round [8, 9] and rectangular [11, 12] nozzles operating with and without the addition of afterburner.

One perceptual feature of jet noise is crackle, which has been described as an annoying [13] and dominant [14] component of full-scale jet noise. This perceptual feature has been related to the reception of acoustic shocks, indicated by the skewness of the pressure time derivative, or derivative skewness ($\text{Sk}\{\partial p/\partial t\}$) measured at the listener location [15–17]. These studies have identified a crackle rating system that describes the perceived crackle in the field, which is noted here in Table 1. Reporting the derivative skewness lends insight into the potential for crackle perception in communities near air bases.

Table 1   Rating scale for perceived crackle content from Ref.[15].

$\text{Sk}\{\partial p/\partial t\}$ Approximate Lower Bound	Description
<0.3	Smooth noise; no crackle
>0.3	Rough noise; no crackle
>1	Sporadic crackle
>3	Continuous crackle
>9	Intense crackle

The layout of the remainder of the paper is as follows. First, Section III discusses the measurement procedure, microphone arrangement, and data acquisition systems used. Then, Section IV discusses minor complications of the measurement due to additional sources of noise and data acquisition limitations. Sections VI, VII, and VIII discuss measurements of the near-field imaging array, the influence of the ground reflection on off-ground measurements, and measurements by the far-field arrays. Overall sound pressure levels (OASPL) under and around the aircraft and spatial maps of select one third octave band levels are included in the Appendix.

III. Measurement Description

A. Measurement Procedure

The measurement was conducted early in the morning on August 18th, 2019 at Holloman Air Force Base in New Mexico. The aircraft was tied-down to a concrete run-up pad which extended 12.2 m (40 ft) to either side of the aircraft and far downstream. The origin of the coordinate system used is directly under the nozzle exit on the ground, with the positive *x*-direction downstream of the nozzle, negative *x*-direction upstream towards the nose of the aircraft, positive *y*-direction on the array side (port side of the aircraft), and positive *z*-direction as the height above ground. The nozzle center was approximately 1.65 m (65″) above the ground, though this varied slightly (±5 cm) throughout the test as the pitch of the aircraft compensated for the changes in engine power. A microphone array reference point (MARP) located 13′ downstream of the nozzle was established to determine angles, θ, relative to the jet inlet with 0° pointing upstream towards the nose of the aircraft and 180° pointing downstream along the jet centerline.

The aircraft was cycled through various engine conditions multiple times, pausing at each condition for at least enough time for each data acquisition system to record for 30 seconds. An ambient measurement was first taken before startup, then the APU startup sequence initiated and ran until fully prepped for engine startup. The engine was then started and ran at idle. Then, the engine was run at N2 values of 75%, 82%, 88%, and at full military power, then with

afterburner. After 30 seconds at afterburner, it was brought down to idle for a few minutes, then the cycle from 72% N2 to afterburner was repeated and finally powered down. This complete sequence was repeated two additional times, giving at least six measurements of each test point. For the purposes of this paper, results from 82%, 88%, Military power, and Afterburner will be shown.

B. Microphone Arrangement

Over 200 microphones were organized into various arrays from the immediate vicinity of the aircraft out to 229 m (750′), as shown in Fig. 1. Eleven locations under and around the aircraft were measured using a set of four low-sensitivity GRAS 40BG 1/4″ pressure microphones on tripods which were moved between measurements to cover all the locations (numbered orange circles). Four low-sensitivity GRAS 40BH 1/4″ pressure microphones were placed approximately parallel to the shear layer of the jet and taped to the ground. Farther out, a 120-channel array (referred to as the "Imaging array") of GRAS 46BD and 46BG 1/4″ pressure microphones were taped to the ground, ranging from $x = -15.2$ m (50′) to $x = 53.0$ m (−174′) (gray circles in Fig. 1b). Downstream of the nozzle, the array was linear, starting at $y = 17′$ and extending aft approximately parallel to the shear layer. Upstream, the array linearly increased in y for several feet then extended upstream parallel to the jet centerline. The inter-element spacing of the array varied based on predicted peak frequencies of the aeroacoustic noise, such that the spacing was smaller towards the sideline of the jet where higher frequency components were predicted to dominate and larger in the aft, where the louder, lower frequency components were predicted to dominate. On the concrete run-up pad was also a line array 7.62 m (25′) parallel to the jet centerline, which spanned from $x = -21.34$ m to $x = 18.29$ m (light green circles in Fig. 1b). Special low-sensitivity GRAS 40BE-S2 free-field microphones, which have been used on previous measurements of high-performance aircraft [7] were mounted on tripods 1.52 m (5′) off the ground.

Beyond the run-up pad, there were five microphone arc arrays centered around the MARP with radii of 19.1 m, 38.1 m, 76.2 m, 152 m, and 229 m (63′, 125′, 250′, 500′, and 750′), corresponding to dark blue, red, green, purple, and yellow circles in Fig. 1a. The 19.1 m and 38.1 m (63′ and 125′) arcs consisted of GRAS 40BE-S2 microphones, whereas the remaining arcs used 1/4″ GRAS 40BE and 46BD microphones, all of which which were mounted 1.52 m (5′) off the ground. The 19.1 m, 38.1 m, and 76.2 m (63′, 125′, and 250′) arrays ranged from 30° to 160° in 10° intervals, with additional locations in 5° increments from 110° to 160° for the 76.2 m (250′) arc. Additional arc arrays at 152 m and 229 m (500′ and 750′) are more sparse with locations at 40°, 90°, 110°, 120°, 130°, 135°, 140°, 150°, and 160°. At these two outer arcs, the terrain became significantly more uneven and overgrown with brush, sometimes as tall as the mounted microphone height.

Other than the aforementioned arrays, additional measurements were taken to investigate the effect of microphone height on the measured sound field and the influence of the ground reflection on the perception of crackle. Two such setups on the concrete run-up pad were placed at 130° and 150° and included GRAS 1/8″ 40DD microphones mounted on the ground as well as at 2.54, 7.62, and 15.24 cm (1″, 3″, and 6″) heights, with GRAS 1/4″ 46BD microphones at 0.305 and 1.52 m (1′ and 5′) heights. These locations are shown as the light blue dots on Fig. 1b).

C. Data Acquisition

The microphones comprising the Imaging array and the near-field line connected to a large National Instruments PXIe 24-bit system populated with 449x series 16-ch cards and 4462 4-ch cards. To simplify cabling, 4X infiniband cables were used to run from the acquisition system to the arrays and custom infiniband to BNC breakout boxes attached to connect the individual channels to the infiniband cable. The system provided 4mA constant current power to the prepolarized microphones, and was able to sample all 120+ channels at a 204.8 kHz sample rate over a ±10V range. The PXIe chasis was controlled by a NI-8354 server with two internal and one external solid state drives for data storage.

The 7.62 m (25′) line array as well as the 19.1 m, 38.1 m, and 76.2 m arc arrays and the roving maintainer microphones were run via BNC and Infiniband cable to a National Instruments PXIe-1062Q chasis with 4496 and 4497 cards as well as an 8840 Quad Core Controller. The 100+ channels were intended to be sampled at 204.8 kHz as well, though limited hard-drive write speeds required that the sample rate be changed to 96 kHz partway through the test. A 4mA constant current power supply over ±10V input range was used for this acquisition system as well. The controller was operated via remote desktop connection from a laptop to manage the recording process.

The microphone height study on the run-up pad were connected via Infiniband cable to a third PXIe chasis loaded with two 6-ch 24-bit National Instruments PXIe-4480 cards. This was controlled by a laptop via expresscard that sampled the twelve channels at 1.024 MHz over a ±10V range with capacity for 10mA constant current power.

To avoid excessive cable runs to the 152 m and 229 m arc arrays, the 18 channels were collected using seven

3
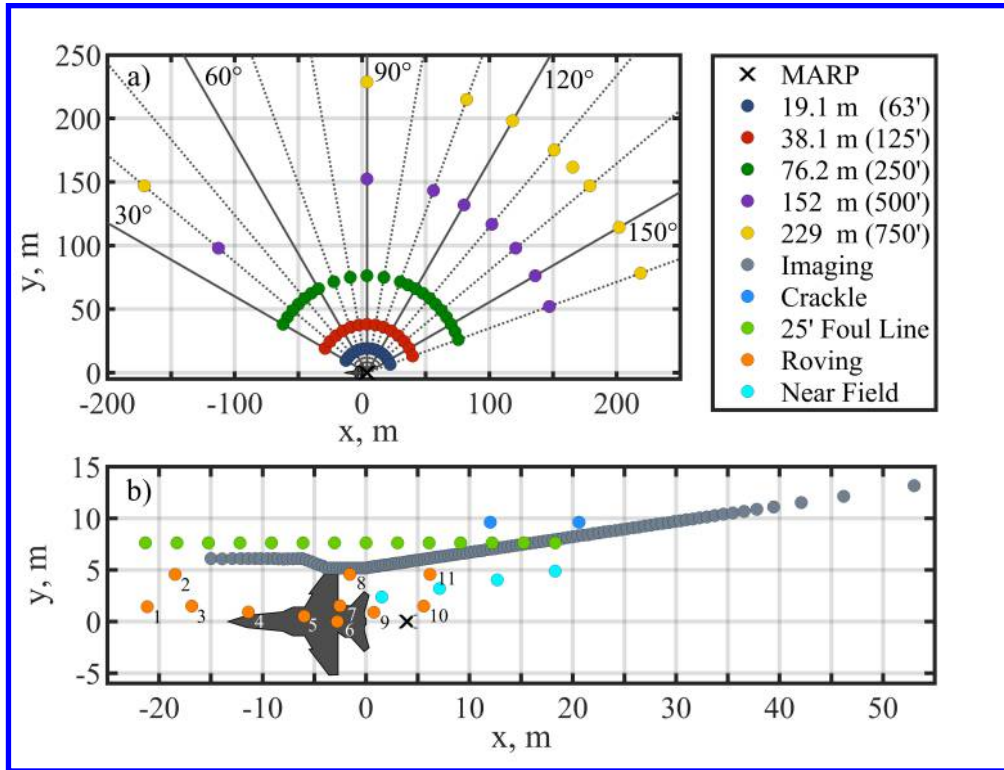
Fig. 1   Measurement schematic of the T-X for the a) far-field microphone arcs and b) near-field microphone arrays. Angles are defined relative to the jet inlet and centered about the microphone array reference point (MARP) with solid and dashed lines every 30° and 10°, respectively. Though the array was physically placed on the port side of the aircraft, it is shown mirrored in this figure for plotting convenience.

individual data acquisition systems placed in the field near their respective microphones. They were comprised of National Instruments 9250 2-channel cards mounted onto 9174 cDAQ 4-slot USB chassis, which were plugged into small tablet PCs. The fixed ±5 V, 2 mA data acquisition systems, computers, and IRIG-B timeclocks were all powered by MAXOAK lithium-ion batteries, creating a compact, portable data acquisition unit. Each tablet PC also connected via Bluetooth to Kestrel 4500 weather meters, which simultaneously recorded ambient weather data.

The total of 10 independent data acquisition systems used IRIG-B GPS timeclocks to allow for post-process synchronization of the recordings. All the systems were managed using the custom Acoustic Field Recorder (AFR) software developed by Brigham Young University and Blue Ridge Research and Consulting LLC. This robust software has been used on previous jet noise measurements [7, 8], measurements of weapon noise [18], rocket launches and test firings [19, 20] and sonic booms, and is designed for efficient configuration, rapid deployment, and highly scalable systems. It includes options for both level and time-based triggering, and allows for real-time monitoring of levels, spectra, and other statistics.

D. Weather

In addition to acoustic data, several weather stations, such as the one pictured in Fig. 2e, recorded the ambient temperature, relative humidity, and wind speed over the course of the measurement. The measurement was conducted early in the morning (5-7 am local time) to avoid high wind speeds. The temperature and relative humidity varied from 19.9 - 25.8 °C, 21.9 - 31.9 %, while the average wind speed was 1.9 kts over the course of the measurement.

IV. Data validation

Given the large number of the number of channels used in this measurement, some subset would inevitably have issues. Upon analyzing the recordings, a few non-acoustic signals were found corrupting some of the collected pressure

Fig. 2 Images of T-X measurement layout at Holloman Air Force Base, New Mexico: a) tied-down aircraft with 38.1 and 19.2 m (125′ and 63′) **arcs and maintainer mics visible, b) imaging ground array and maintainer mics facing downstream, c) 130° crackle station facing a loudspeaker located at the MARP, d) imaging array data acquisition unit, and e) Kestrel weather station located at 57.2 m** (187.5′) **along the 70° radial.**

waveforms. At the data acquisition system capable of sampling up to 1.024 MHz, Electromagnetic noise of unknown origin appears when sampling the voltage at a rate high above the roll off frequency of the microphone. Along the Imaging array, intermittent voltage spikes are seen on a few seemingly random channels during some power cycles of the aircraft. Additionally, ten of the 120 channels used in the imaging array experienced preamplifier saturation, where the slew rate of the data acquisition system was insufficient to provide the power needed to represent the acoustic signals at the afterburner condition. Sections IV.A and IV.B discuss identification and elimination of these non-acoustic signals.

A. Electromagnetic noise

The first instance of non-acoustic electrical noise was observed only at the data acquisition system that sampled at 1.024 MHz. The corresponding Nyquist frequency is well above the high-frequency roll off of the microphones (about 80 kHz). This noise presents itself throughout the time waveform as sinusoidal pulses. A simple low-pass filter (or resampling the waveform to a lower sampling rate) is sufficient to remove these artifacts.

Recordings collected in the far-aft portion of the imaging array also contain electronic noise but of a different nature. These consist of spikes in the time domain, as shown circled in red for channel 300 in Fig. 3a). However, the adjacent channel, which has been time-aligned using a cross correlation, does not have these spikes in the waveform. For 82% N2, only 2 of the 6 runs have this type of noise, and occurs on about 20 - 24 channels of the 120 channels. At higher engine conditions, 3 of the 6 runs have this type of noise, and is only significant for 3 - 12 channels. What is curious about this noise is that it does not consistently affect a particular channel nor small group of adjacent channels, and seemingly appears in a random assortment of individual measurements. For all cases, however, it appears to be limited to microphones on the imaging array downstream of x = 20 m.

While these spikes appear to not have any significant impact on some metrics, such as OASPL, they can drastically impact statistical values including the Sk$\{\partial p/\partial t\}$ and the kurtosis of the time derivative of the pressure waveform, Kurt$\{\partial p/\partial t\}$. For a particular measurement, channels with these intermittent spikes can be identified by examining the Kurt$\{\partial p/\partial t\}$, which will report unexpectedly large values. Fig. 3b) shows the Sk$\{\partial p/\partial t\}$ and the Kurt$\{\partial p/\partial t\}$ along the imaging array for a single measurement at 88% N2. For the purpose of this paper, the Sk$\{\partial p/\partial t\}$ is not reported for data contaminated with this noise. Excluded data is determined using the Kurt$\{\partial p/\partial t\}$ on the following criteria. For measurements without any of this noise present at 82% N2, the maximum Kurt$\{\partial p/\partial t\}$ is only slightly leptokurtic with a value of about 4, so all channels downstream of 20 m that exceed this value are excluded when reporting the Sk$\{\partial p/\partial t\}$. For 88% N2 and greater engine powers, the Kurt$\{\partial p/\partial t\}$ is much greater, so any data point for which
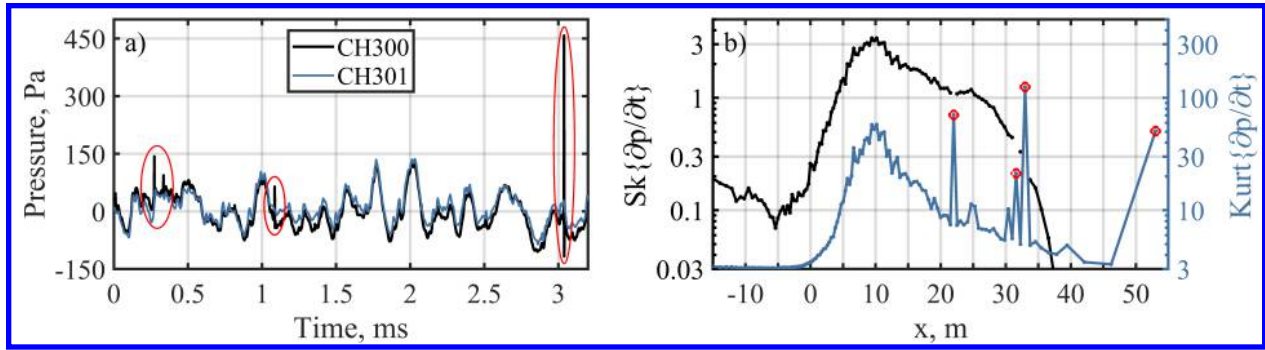
Fig. 3 a) Example waveforms with and without non-acoustic spikes circled in red and b) Sk{$\partial p/\partial t$}and the kurtosis of the time derivative of the pressure waveform, Kurt{$\partial p/\partial t$}, along the imaging array for a single run at 88% N2.
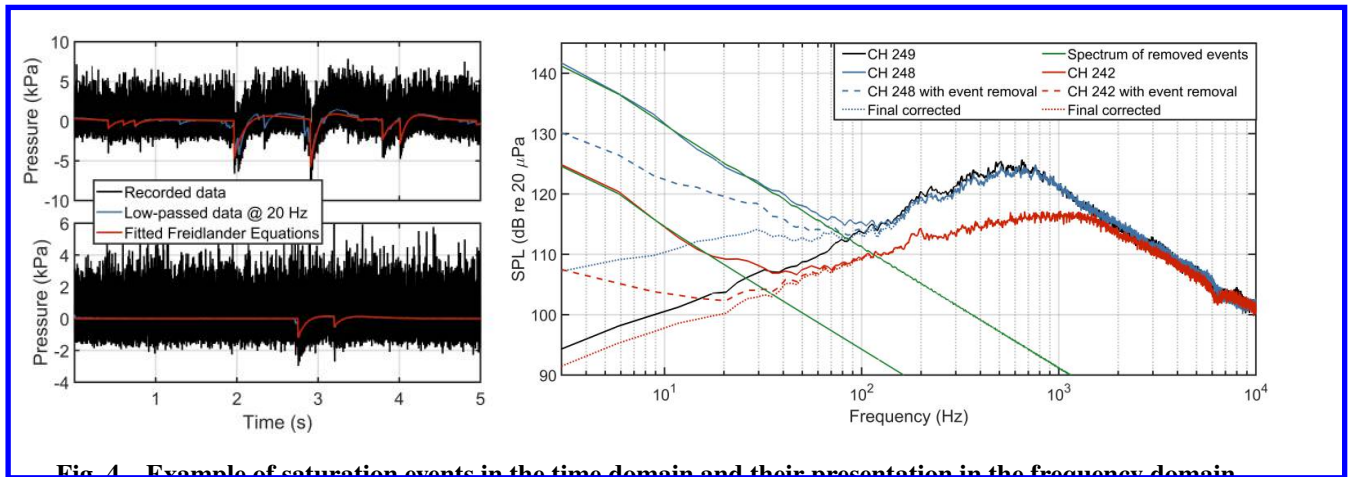
Fig. 4 Example of saturation events in the time domain and their presentation in the frequency domain

the Kurt{$\partial p/\partial t$}value deviates from values at spatially adjacent locations by more than the standard deviation of the Kurt{$\partial p/\partial t$}across the array is eliminated. This does not get rid of all potentially contaminated data, but as shown in Fig. 3b), excludes the extrema circled in red. These criteria are applied to 3 of the 6 runs, for which there are non-acoustic spikes present in the pressure waveforms.

B. Saturation

The high-amplitude jet noise in conjunction with the high frequency content present in the acoustic shocks provides a challenge for measurement. As noted in Section III, microphones were selected with low input sensitivities so that voltages recorded by the data acquisition systems would remain within allowable limits, however, even when within the voltage limits, the acquisition system can only supply a finite amount of power to the microphone, described by the "slew rate". If too large of changes occur in the pressures over too short of periods of time, the acquisition system cannot supply enough power to the microphone, causing the capacitance of the microphone-preamplifier-cable system to discharge. This causes the superposition of a large negative pulse to the voltage waveform which settles back to the mean value over a large time scale compared to the acoustic signal. This is called a preamplifier saturation event, and has been seen in prior measurements of rocket noise [21] and in acoustic pyroshock data [22]. Examples of this phenomenon are in the left plot of Fig.4. Two portions of waveforms with more (top, channel 248) and less (bottom, channel 242) severe saturation events are seen with the sudden, drastic change in the local mean value. Since this event is long compared to the period of the majority of the energy present in jet noise, it is easy to pick out visually. Depending on the severity of the incident, the pulse either settles back to the mean value directly and can be modeled as a decaying exponential function, or it overshoots the mean value once and then decays back over an even longer time period. In the latter case, the Freidlander equation (a commonly used equation to model the overpressure of blast waves) fits the event shape quite nicely.

6

The spectrum of a Freidlander pulse with the time scales observed in this measurement is nearly linear on a log scale, with large amplitudes at low frequency and decreasing at about 20 dB/decade. Therefore, it is also easy to observe the presence of saturation in the frequency domain. The right plot of Fig. 4 shows the spectra of three different channels: 242, 248, and 249. Channel 249 was a GRAS 40BG microphone with a sensitivity of 0.29 mV/Pa, while channels 242 and 248 were GRAS 46BD microphones with sensitivities of 1.2 and 1.1 mV/Pa respectively. Channel 249 did not contain any saturation events because the low sensitivity caused the high pressures to translate to lower voltages (and less required power output) on the data acquisition system. Channel 248 recorded many more saturation events than channel 242 because it was located farther aft of the aircraft and experienced higher levels. The saturation events dominate the jet noise spectrum from DC all the way up to almost 150 Hz for the channel 248 and from DC to almost 70 Hz for channel 242.

Possible solutions to remove these events depends on the number of saturation events present in the signal. If only few events are present, an algorithm can be easily written to search for these events, fit a decaying exponential or Freidlander wave to the event, and then subtracting the fitted function from the time waveform. However, if there are so many saturation events that they significantly overlap this problem begins to be non-trivial. Success or failure of removing all the events then depends on the time dedicated to writing a robust enough algorithm to catch all the events and accurately perform the fits. In any case, if specific time domain information (such as the exact amplitude of the acoustic shock which caused the saturation event) is not needed, and spectral content is not needed at these low frequencies, a simple high-pass filter can be employed to eliminate the effects of the saturation on statistical quantities such as the mean and variance. A first attempt at a fitting algorithm was applied to the affected recordings in this work, and the results are shown in Fig. 4. On the left, superimposed on the time waveforms is the low-pass filtered waveforms with a cutoff frequency of 20 Hz (blue) as well the fitted Freidlander equations (red) produced by the algorithm. In the top plot, where the saturation events were more severe, the algorithm was unable to fit all of the events, or fit a single Freidlander equation over two overlapping peaks. The spectra of channels 242 and 248 after the events were removed are shown as the dashed lines on the right of Fig. 4, as well as the spectra of the removed events themselves in green. The removal method was able to reduce the influence of the saturation events to below 80 Hz for channel 248 and below 35 Hz for channel 242.

Among the ten channels that experienced these saturation events, there varied from as little as a single event during a 30 second measurement to a few hundred events. For channels where the event finding algorithm was insufficient to completely fix the spectra (as displayed by the dashed lines in Fig. 4), the waveform was then high-pass filtered with a 1st-order Butterworth filter (to mirror the 20 dB per decade slope of the saturation events) with the cutoff frequency at the intersection of the spectrum of the Freidlander events (green lines) with the recordings after event removal (dashed lines). The dotted lines show the effect of the addition of the filter, which seems to effectively eliminate saturation issues for moderate cases exemplified by channel 242, and bring down the effect of severe cases exemplified by channel 248 enough that further preliminary analyses of these recordings can be undertaken.

V. Sampling Rate considerations

Previous studies [23, 24] have commented on the importance of using a high sampling rate to accurately represent the sharp rise times of acoustic shocks present in the time waveform of aeroacoustic noise. Though the ANSI/ASA standard S12.75 recommends at least 96 kHz, 204.8 kHz has been used in the past for high-performance military aircraft measurements [7, 8]. Of particular interest is the calculation of the skewness of the time derivative of the pressure, Sk$\{\partial p/\partial t\}$, which can be used to predict the perception of crackle. To test the effect of the sample rate on the Sk$\{\partial p/\partial t\}$, the data obtained in the region of maximum radiation by the Crackle array was systematically downsampled from 1.024 MHz to 10 kHz and the Sk$\{\partial p/\partial t\}$ calculated each time, which is plotted in the left portion of Fig. 5. The vertical axis is the calculation of Sk$\{\partial p/\partial t\}$ displayed on a logarithmic scale, and the horizontal axis is the sample rate. Each colored line is the mean value across the measurement for a given engine condition and location, solid lines at 130° and dashed at 150°.

At the full 1.024 MHz sample rate, the Sk$\{\partial p/\partial t\}$ was actually lower than anticipated, which was due to the non-acoustic components at high frequency discussed in section IV.A. Once downsampled enough to effectively filter out the non-acoustic noise, the Sk$\{\partial p/\partial t\}$ takes on a mostly constant value until about 150 kHz, where the Sk$\{\partial p/\partial t\}$ begins to monotonically decay as sampling rate is continually decreased. The response of the majority of the microphones used in this measurement begin to roll off around 80 kHz, so it makes sense that after the sample rate is sufficiently high to record everything the microphone is able to detect, the Sk$\{\partial p/\partial t\}$ would not change much.

However, many of the measurement channels were restricted to a 96 kHz sample rate. The right portion of Fig. 5

7
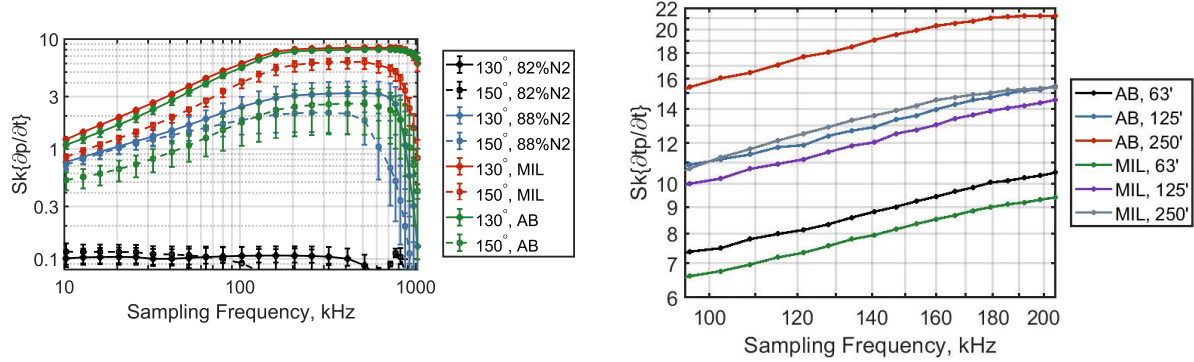
Fig. 5   Derivative skewness values at varying downsampled frequencies for three engine conditions at two 5′ mic locations

plots the Sk$\{\partial p/\partial t\}$ at military power and afterburner at 120° at three different radial distances from the MARP, and how the values change as a function of sample rate from 96 kHz to 204.8 kHz. in each case, there is a fairly linear trend which shows an underestimation of the Sk$\{\partial p/\partial t\}$ at 96kHz by about 30%. For the preliminary analyses in this work and for the sake of averaging across multiple measurements at the same engine power, all waveforms were downsampled to 96 kHz, so the Sk$\{\partial p/\partial t\}$ values reported hereafter should be regarded in light of the fact that their true values are underpredicted by as much as 30% in the region of maximum radiation.

VI. Near-field

Pressure measurements along the Imaging Array give a detailed look into the geometric near field of the noise produced by the aircraft. Figure 6 shows the OASPL and skewness of the pressure derivative, Sk$\{\partial p/\partial t\}$, measured along the array for each measurement for four engine conditions. The variance between measurements is minimal upstream of $x = 25$, though towards the end of the array it becomes large, with pairs of measurements clustering together separate from others. As stated in section III.A, the aircraft powered on, cycled through engine conditions twice, then powered off again. Additional analysis of the exact operating parameters of the engine as well as variance of the weather conditions is needed to understand why individual power cycles would cluster the way they did. For the purposes of this paper, however, all subsequent figures will display the mean of the statistical quantities over the 6 runs.

Figure 7 shows the spectra (from 0 to 2000 Hz) recorded at each microphone along the 120- channel Imaging Array arranged by the x-coordinate of the measurement position. The squared pressures of the spectra are averaged over the 6 runs, and the entire plot is normalized to its peak value for each engine condition to share a common color scale. The engine power and maximum SPL is recorded in the upper right corner of each pane. Colors change in 1 dB increments with contour lines every 6 dB. As has been shown in previous measurements of other high-performance military aircraft, this measurement contains spatiospectral lobes, or local maxima and minima in the space-frequency domain plotted in Fig. 7. There is a definite change of structure as engine power is increased among the intermediate conditions, in this case from 82% N2 to 88% N2, where additional high-frequency spatiospectral lobes appear upstream of the main radiation lobe. This mirrors the pattern in the OASPL seen in Fig. 6, where there is a large increase in the forward portion of the OASPL between 5 and 10 m downstream.

Generally, the spectra follow classical trends in jet noise, with broad spectra towards the sideline and more peaked spectra towards the aft, with the addition of broadband shock associated noise, BBSAN, radiating in the forward direction at the higher engine powers. However, at all engine powers significant deviations from this norm appear in the aft radiation, where multiple peaks in the spectra are seen. The spatiospectral shapes seen in Fig. 7 are qualitatively similar to those seen in a similar measurement taken of an F-35B [10, 25].

VII. Influence of the ground

The Near-field measurements discussed in the previous section were all located on the ground, while the mid to far-field measurements were all taken at a height of 5′. A first order estimate of the effect of the ground would be a perfect pressure doubling, representing an increase in the OASPL by 6 dB. The measured difference in OASPL between
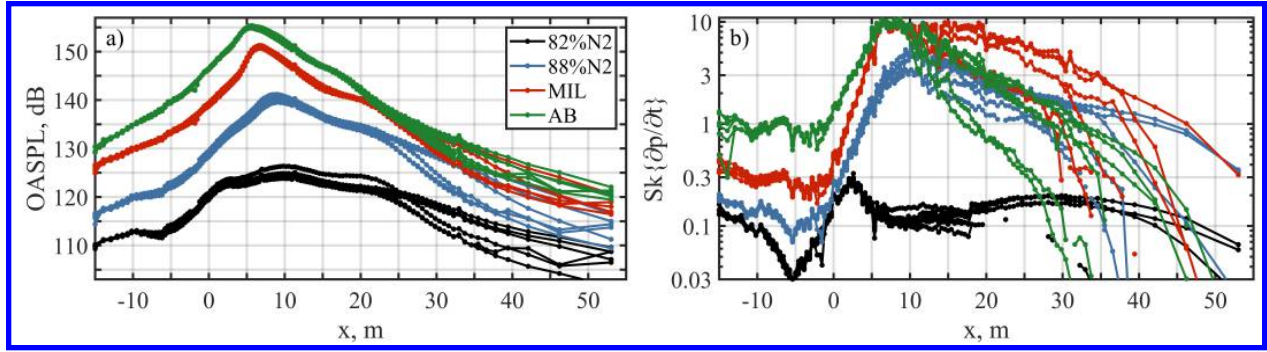
Fig. 6 a) Overall sound pressure level and b) Sk{$\partial p/\partial t$} values calculated along the imaging array for each measurement at four engine conditions
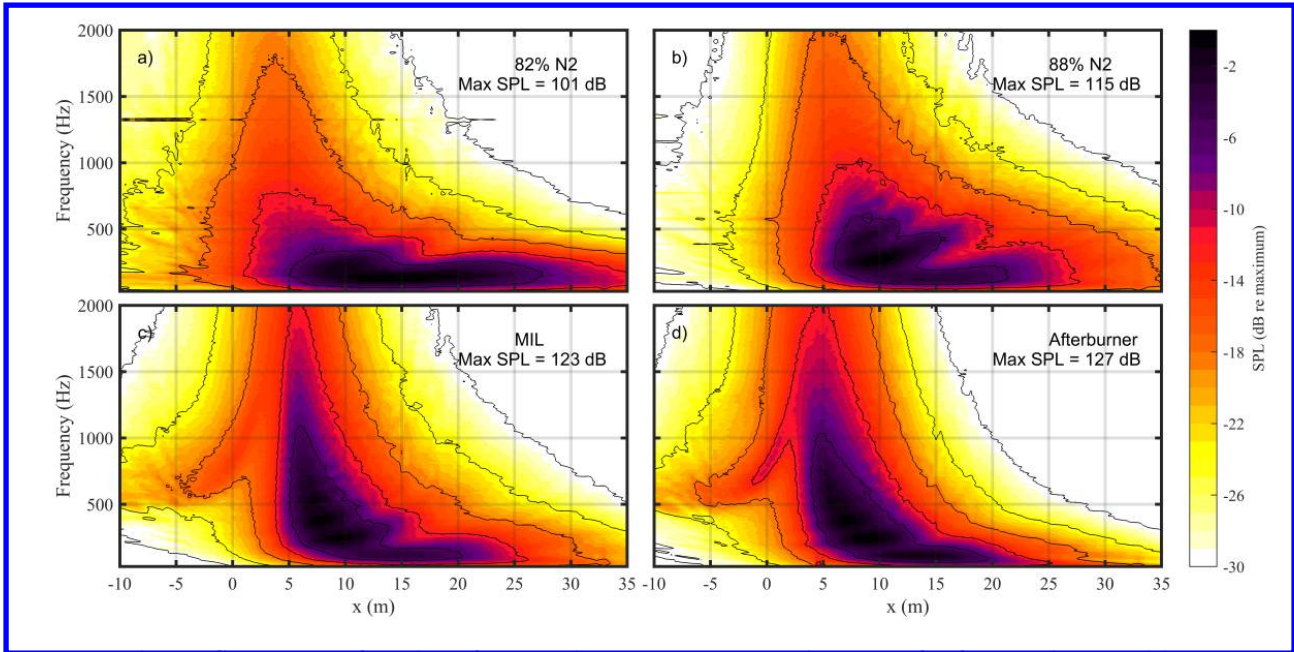
Fig. 7 Spectra as a function of x-coordinate along the imaging array for four engine conditions

co-located ground and 5′ microphones are given in Table 2, which shows for two different angles the mean and standard deviations of the OASPL differences for the four engine conditions. The OASPL is greater at the ground, though the difference is as low as 1.1 dB for Afterburner at at the 150° location and as much as 4.4 dB at the 88% N2 condition at the 130° location.

Comparison of the ground and 5′ spectra at these different conditions and locations sheds insight into the variance of the OASPL differences. Figure 9 shows the spectra at these locations (arbitrary amplitude, offset for clarity) and engine conditions. The solid lines are the spectra measured at the ground and dashed lines measured at 5′. The largest differences in OASPL between the ground and aerial microphones is where the ground reflection null appears at the peak in the spectrum. Because of the frequency-dependant and ambiguous source geometry, very deep nulls are not seen in the ground reflection spectra for many configurations, resulting in much smaller than expected OASPL reductions in the aerial microphones.

VIII. Far-field

The remainder of the presented results were measured 5′ off the ground in the mid to far-field of the aircraft, starting with the 25′ foul line and including the 19.1, 38.1, 76.2, 152, and 229 meter arc arrays. First, two-dimensional maps of the OASPL and Sk{$\partial p/\partial t$} are generated by interpolating between the measurement points. Figure 10 shows the
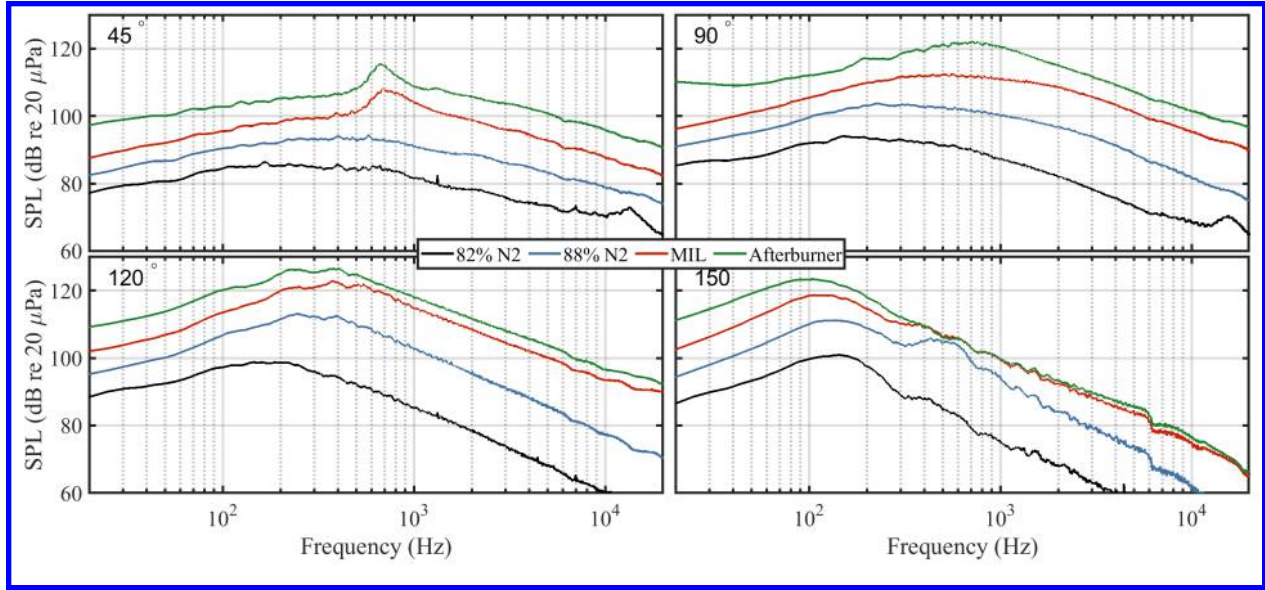
Fig. 8 Example mean spectra measured along the imaging array at four different inlet angles and engine conditions

Table 2 Average OASPL difference between co-located microphone at ground and 5′ heigths for the two Crackle Study measurement locations, denoted by angle, and standard deviations averaged across 6 runs.

Angle	82% N2	88% N2	MIL	AB
130°	3.0 ± 0.2	4.4 ± 0.3	4.4 ± 0.1	4.2 ± 0.1
150°	1.3 ± 0.2	2.2 ± 0.4	1.7 ± 0.2	1.1 ± 0.2

OASPL measured at four engine conditions, normalized to their respective maximum OASPL as displayed in the title. Measurement points are represented by white dots, and major contour lines are drawn every 6 dB below the maximum with minor contour lines every 3 dB. Consistent with other aircraft measurements, the OASPL increases and the directivity peak shifts towards the sideline with increase in engine condition, with a peak near 150° for 82% N2 and shifting to 120° for Afterburner.

Figure 11 shows the Sk$\{\partial p/\partial t\}$for four engine conditions. The top row of plots are 82% N2 and 88% N2 conditions which share the upper color bar displaying values between 0.02 and 2. Military power and afterburner share the lower color bar with values ranging from 0.2 to 20. Contour lines show breakpoints in the Sk$\{\partial p/\partial t\}$scale for crackle perception categories in Table 1. Due to the sparseness of data points in the far field, linearly interpolated ghost points were inserted along the 152 m and 229 m arcs to aid the interpolation process. As stated in section V, the Sk$\{\partial p/\partial t\}$values in the region of maximum radiation are underestimated by a factor of about 30% due to downsampling to 96 kHz. Similar to the OASPL, the maximum Sk$\{\partial p/\partial t\}$value increases and the directivity peak shifts towards the sideline with increased engine power.

Another visualization of the data gathered along the arcs is shown in Fig. 12. Each column of plots contains the OASPL (top) and the corresponding Sk$\{\partial p/\partial t\}$ (bottom) for a given arc. The horizontal axis is the inlet angle, θ, relative to the MARP. The lines show the mean value across the six measurement repetitions and the error bars represent the minimum and maximum recorded values. Each separate engine condition is represented by a different color, all on the same scale. The variability across measurements for the OASPL and the Sk$\{\partial p/\partial t\}$ is very low for the 19, 38, and 76 m arcs (noticeably lower than the near-field measurements) but increases for the 152 and 229 m arcs, suggesting that that is where meteorological and terrain effects become important to the propagation.

The directivity trends are easier to compare across engine conditions in Fig. 12. Comparisons of the top and bottom rows of Fig. 12 show that the Sk$\{\partial p/\partial t\}$ and the OASPL generally follow similar trends, except for 82% N2 in Fig. 12f) where the Sk$\{\partial p/\partial t\}$ peaks towards the sideline of the jet. For the OASPL, the peak directivity shifts upstream and broadens with engine condition for each arc, though the broadening and upstream shift is less pronounced at the 152
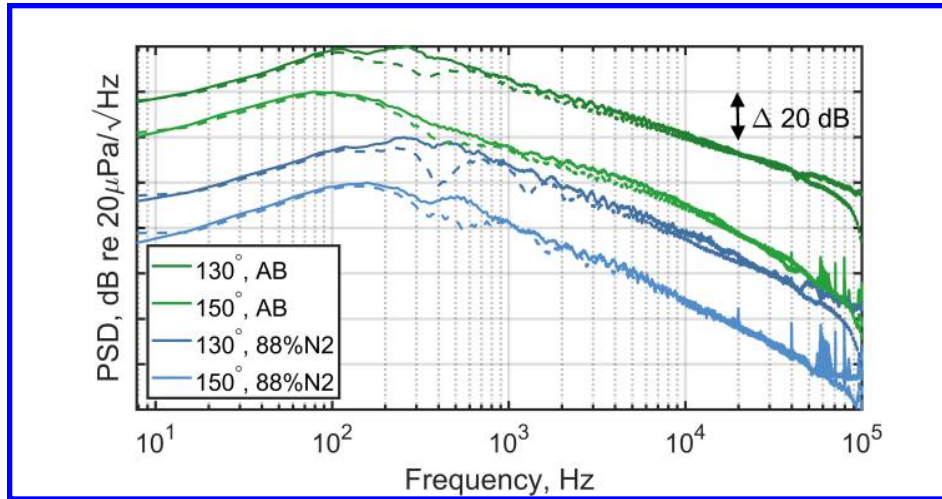
Fig. 9   PSD for 2 heights at 2 engine conditions at 2 locations.   Solid lines denote ground microphone and dashed lines are $5'$ **off the ground.**

and 229 m arcs. For any given location, the OASPL increases with engine power, but at some far aft locations, the Sk$\{\partial p/\partial t\}$ is greater at Military power than at Afterburner. This is partially due to the Sk$\{\partial p/\partial t\}$ peak being more broad at the 19, 38, and 76 m arcs for Military power than at Afterburner.

Propagation trends across different radials are represented by Fig. 13, in the same format as Fig. 12 but each plot shows for a specific inlet angle the OAPSL or Sk$\{\partial p/\partial t\}$ as a function of radial distance. The gray dashed lines in the OASPL plots represents spherical spreading for reference. The OASPL in general follows the spherical spreading curve. A possible contributor for the greatest deviation from the spherical spreading trend in Fig. 13a) for 40° at 152 m may be due to the hard road surface terrain instead of the dirt at the other locations.

The propagation trends for Sk$\{\partial p/\partial t\}$ differs from the OASPL. While the OASPL consistently decays with distance, the Sk$\{\partial p/\partial t\}$ values can increase due to nonlinear propagation [26]. The Sk$\{\partial p/\partial t\}$ for 82% N2 and 88% N2 engine powers either stays relatively constant or decreases with increasing distance from the aircraft, while at Military and Afterburner engine conditions at aft angles the Sk$\{\partial p/\partial t\}$ generally increases with distance. This is likely due to the higher levels that allow for nonlinear propagation effects to steepen the large-amplitude pressure waveforms.

IX. Conclusions

In this paper, we have reported on an extensive measurement of the noise emissions of a T-7A-installed GE F404 engine at four engine conditions. Over 200 microphones were used to capture levels, spectra, and statistical information in the near and far fields. The measurement design and procedures are discussed as well as data post-processing to identify occasional anomalies caused by the harsh measurement environment. Overall repeatability across the six run-ups measured is good, but differences increase at far aft angles. Whether these differences are caused by variations in engine performance or propagation environment remains the subject of future work.

Aside from a prior F-35 static measurement in 2013, this is the most extensive run-up measurement of a military jet aircraft. Beyond far-field directivity analyses, the 120-microphone near-field array offers numerous possibilities for performing similar field and source-related analyses as those performed on previous aircraft. These analyses include spectral decompositions by noise source type, obtaining correlation and coherence functions, deriving source characteristics through holography and beamforming techniques, and reduced-order modeling using wavepackets. Use of similar analysis techniques on the T-7A will allow comparisons against other supersonic jet aircraft. Additionally, the fact that F404 engine nozzles have been used in jet numerical modeling and laboratory experiments allows opportunity to make further comparisons and validate the performance of large-eddy simulations and lab-scale rigs.
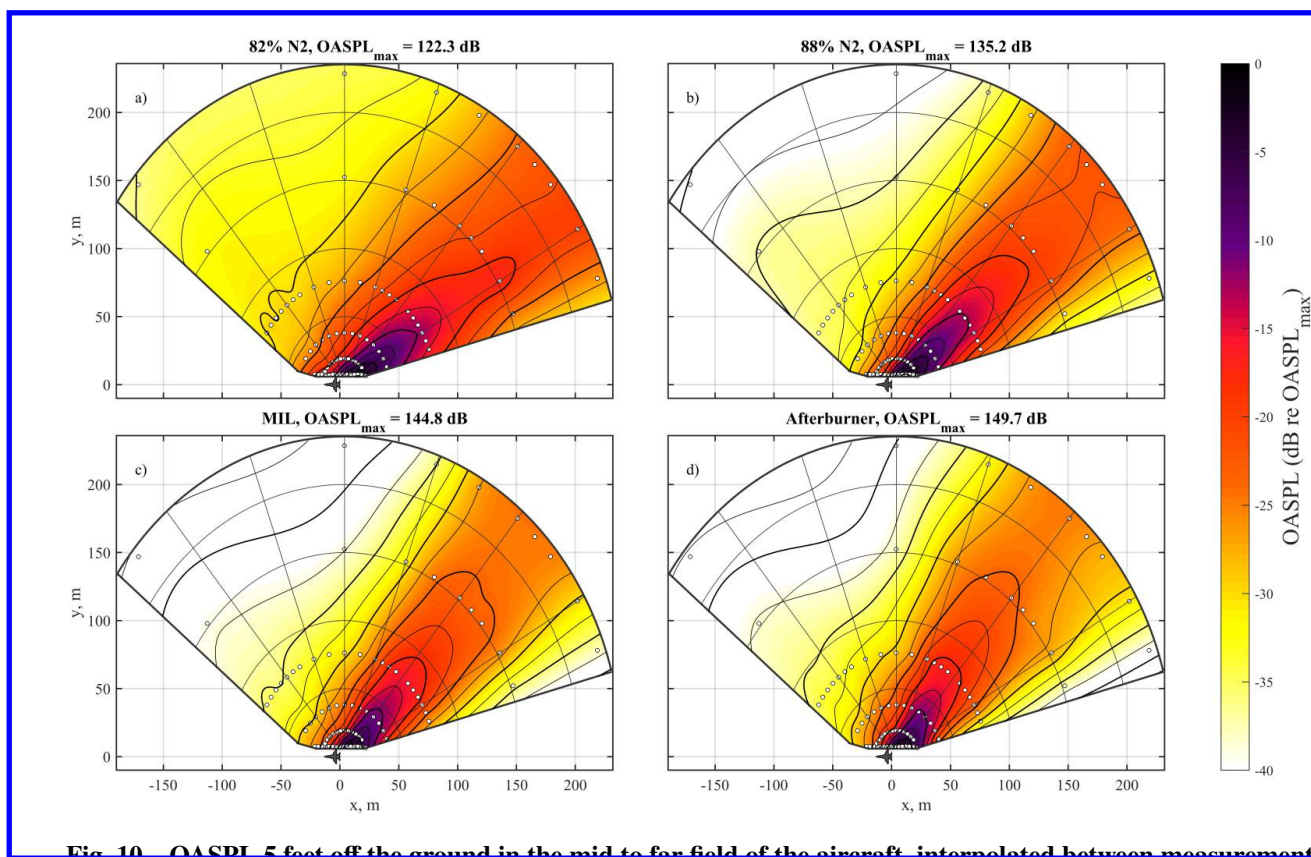
Fig. 10   OASPL 5 feet off the ground in the mid to far field of the aircraft, interpolated between measurement points.
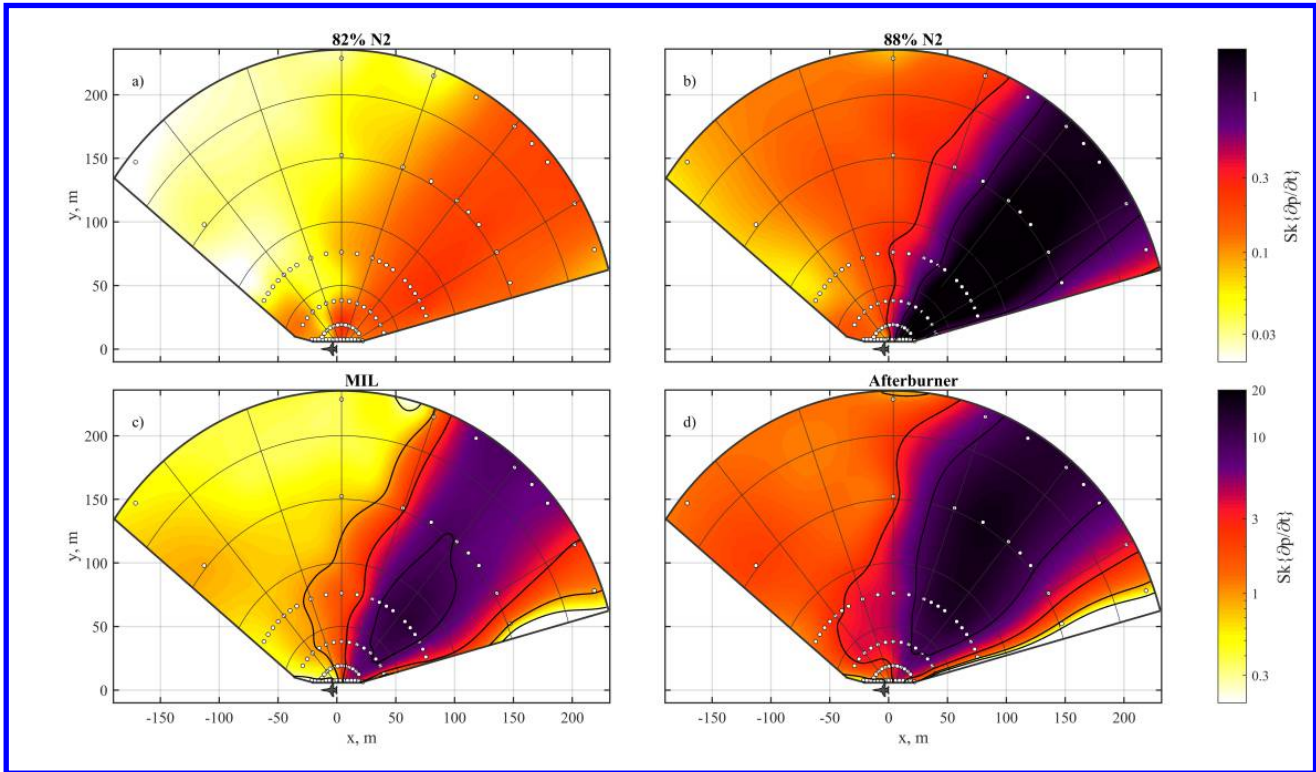
Fig. 11 Sk$\{\partial p/\partial t\}$ 5 feet off the ground in the mid to far field of the aircraft, interpolated between measurement points
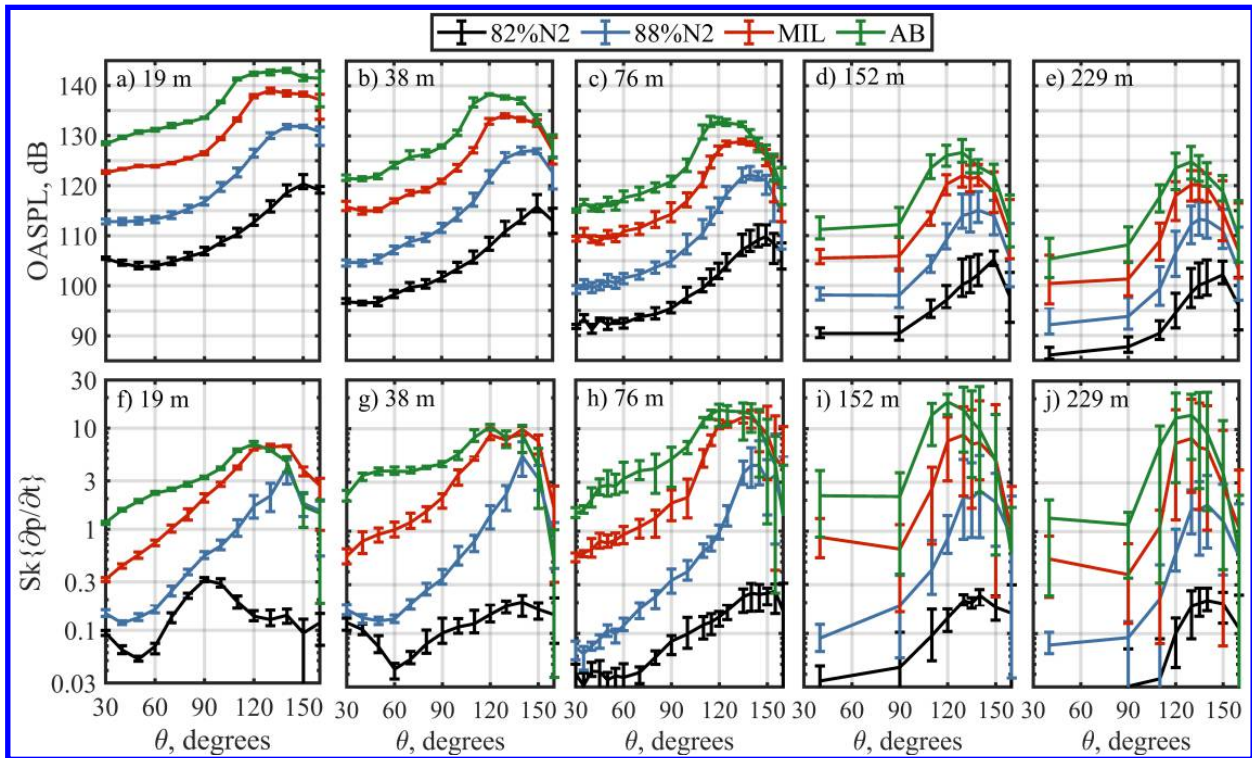
Fig. 12 OASPL directivities for a) 19 m, b) 38 m, c) 76 m, d) 152 m, and e) 229 m arcs and Sk$\{\partial p/\partial t\}$ directivities for f) 19 m, g) 38 m, h) 76 m, i) 152 m, and j) 229 m arcs. Averages across 6 runs are shown with error bars denoting the minimum and maximum values across the runs.

13
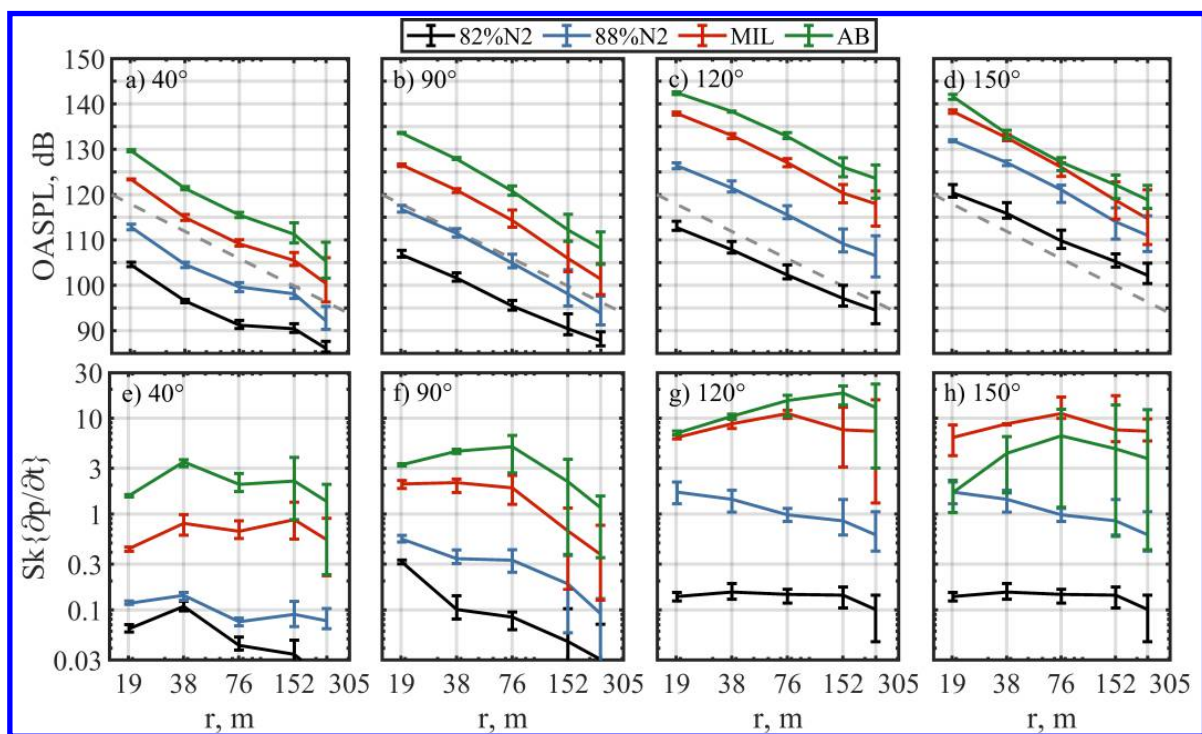
Fig. 13 Spatial OASPL trends along the a) 40°, b) 90°, c) 120°, and d) 150° radials and Sk{$\partial p/\partial t$} trends along the e) 40°, f) 90°, g) 120°, and h) 150°radials. Radial distances are logarithmically scaled and a 1/r decay is shown in a) - d). Averages across 6 runs are shown with error bars denoting the minimum and maximum values across the runs.

Appendix

A. OASPL at Roving Microphone locations

Table 3   Averaged OASPL (dB re 20 μPa) measured at each roving microphone location

Position #	Height	82% N2	88% N2	Military	Afterburner
1	5′	99	105	113	118
2	5′	101	107	115	119
3	5′	103	108	115	119
4	5′	103	108	115	119
5	3′	108	117	127	131
6	3′	111	120	132	136
7	5′	109	118	130	135
8	5′	110	119	129	135
9	5′	125	137	146	153
10	3′	107	116	127	131
11	5′	117	134	145	148

B. Octave Band spatial maps
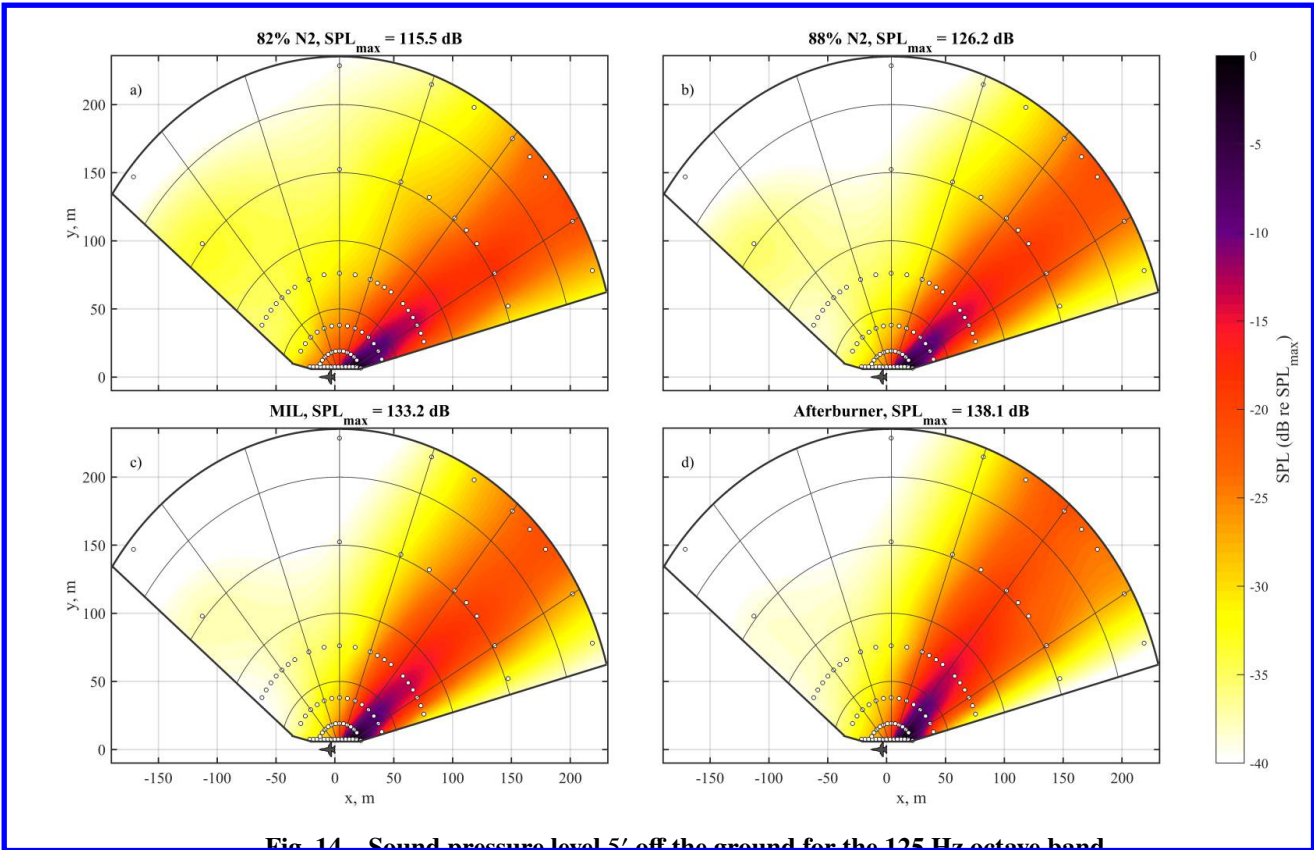
Fig. 14   Sound pressure level 5′ off the ground for the 125 Hz octave band
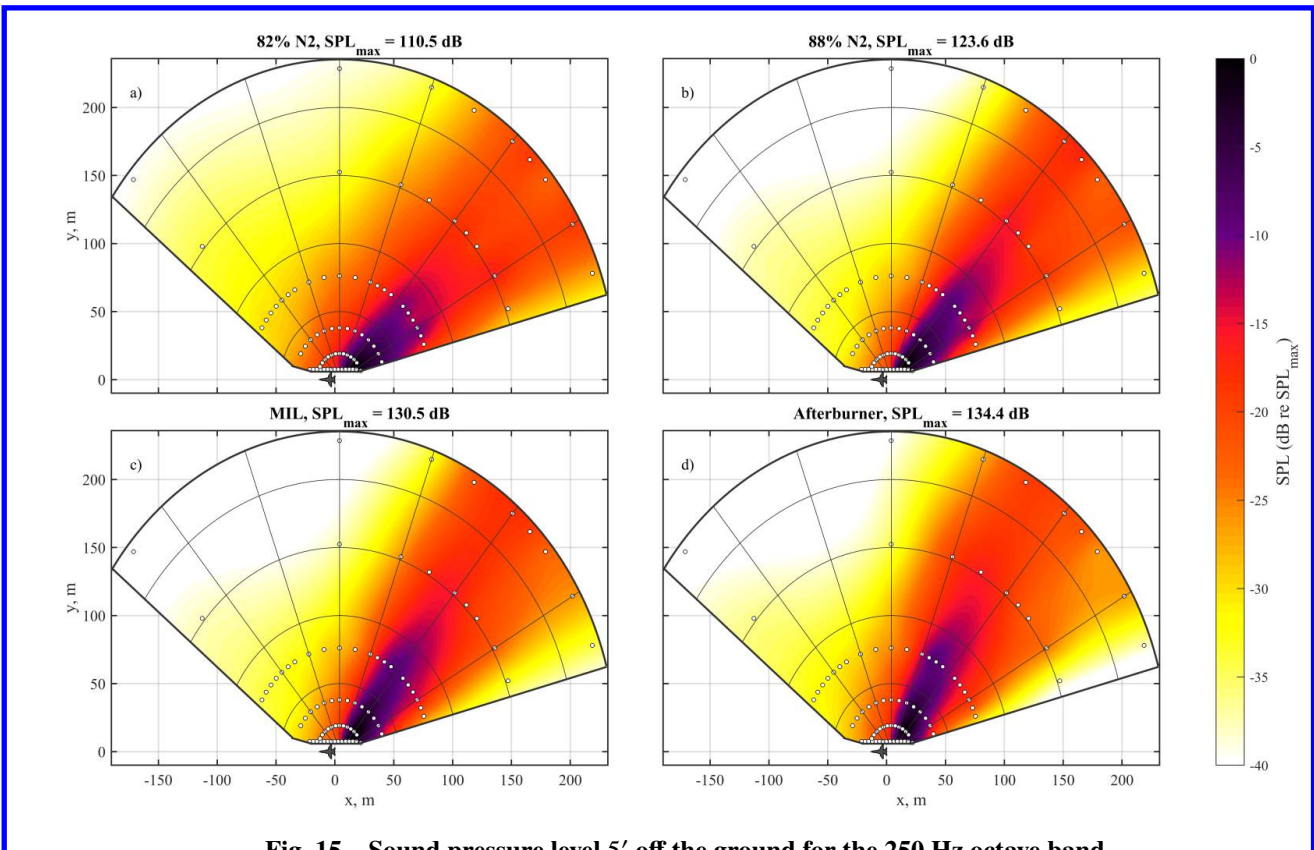
Fig. 15   Sound pressure level 5′ off the ground for the 250 Hz octave band
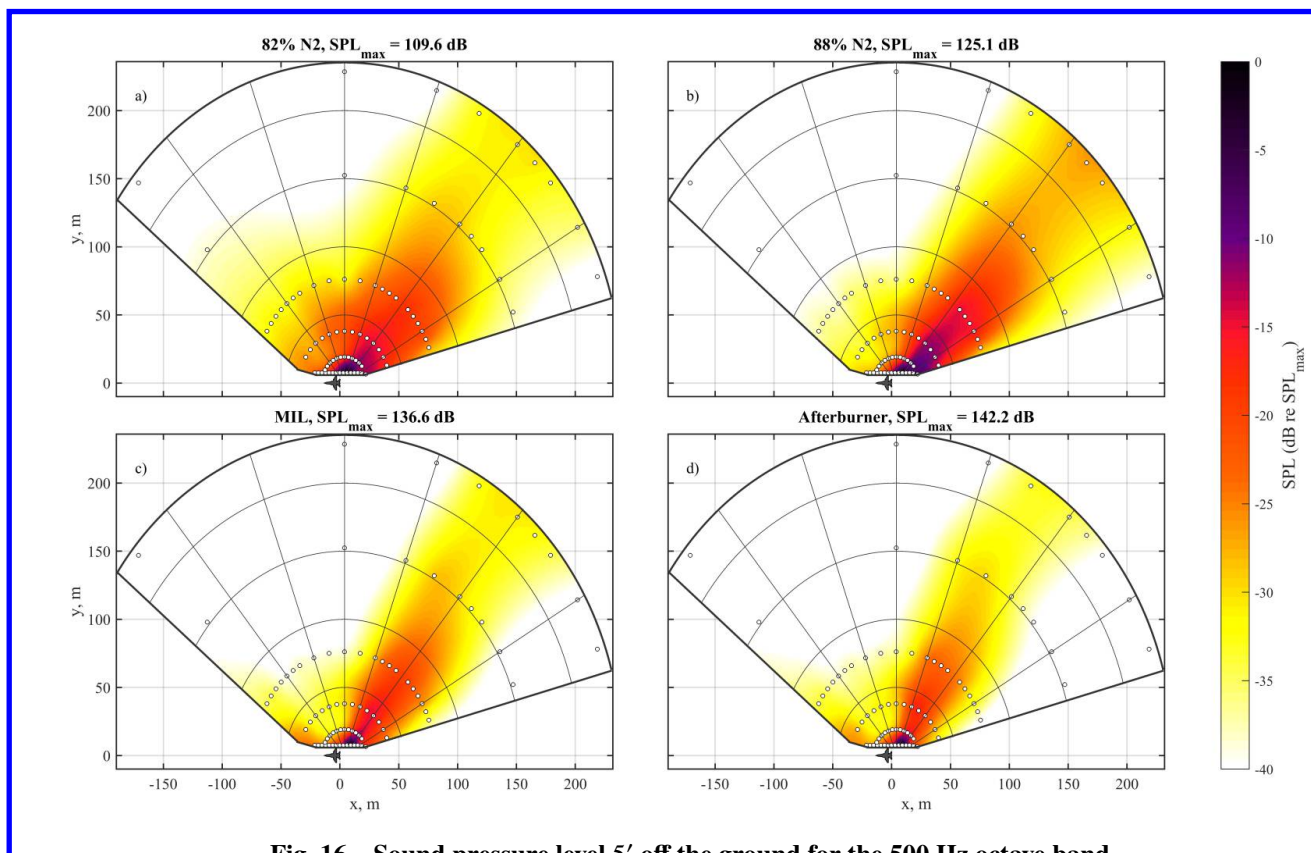
Fig. 16   Sound pressure level 5′ off the ground for the 500 Hz octave band

Acknowledgments

The authors gratefully acknowledge funding for the measurements provided by Advanced Pilot Training System Program Office and the Air Force Research Laboratory. K. M. Leete and R. D. Rasband were funded by an appointment to the Student Research Participation Program at the U.S. Air Force Research Laboratory, 711th Human Performance Wing, Human Effectiveness Directorate, Warfighter Interface Division, Battlespace Acoustics Branch administered by the Oak Ridge Institute for Science and Education through an inter-agency agreement between the U.S. Department of Energy and USAFRL. Distribution A. Approved for public release; distribution unlimited 88ABW-2020-2171; Cleared 07 Jul 2020.

The authors would also like to thank the 586th Fighter Wing at Holloman Air Force Base for the use of the facilities and all the other individuals from various organizations who came together to make this measurement a success.

References

[1] Casalino, D., Diozzi, F., Sannino, R., and Paonessa, A., "Aircraft noise reduction technologies: a bibliographic review," *Aerospace Science and Technology*, Vol. 12, No. 1, 2008, pp. 1–17. doi:j.ast.2007.10.004.

[2] Greska, B., Krothapalli, A., Seiner, J., Jansen, B., and Ukeiley, L., *The effects of microjet injection on an F404 jet engine*, AIAA AVIATION Forum, American Institute of Aeronautics and Astronautics, 2005. doi:10.2514/6.2005-3047.

[3] Seiner, J., Ukeiley, L., and Jansen, B., *Aero-performance efficient noise reduction for the F404-400 engine*, Aeroacoustics Conferences, American Institute of Aeronautics and Astronautics, 2005. doi:10.2514/6.2005-3048.

[4] Murray, N. E., and Jansen, B. J., "Performance Efficient Jet Noise Reduction for Supersonic Nozzles," *International Journal of Aeroacoustics*, Vol. 11, No. 7-8, 2012, pp. 937–956. URL https://doi.org/10.1260/1475-472X.11.7-8.93.

[5] Seiner, J., Jansen, B., and Murray, N., *Aero-performance efficient noise suppression of a supersonic model twin jet nacelle*, Aeroacoustics Conferences, American Institute of Aeronautics and Astronautics, 2009. doi:10.2514/6.2009-3130.

[6] Liu, J., and Ramamurti, R., "Numerical Study of Supersonic Jet Noise Emanating from an F404 Nozzle at Model Scale," *AIAA Scitech 2019 Forum*, 2019. URL https://arc.aiaa.org/doi/abs/10.2514/6.2019-0807.

[7] Wall, A. T., Gee, K. L., James, M. M., Bradley, K. A., McInerny, S. A., and Neilsen, T. B., "Near-field noise measurements of a high performance military jet aircraft," *Noise Control Engineering Journal*, Vol. 60, 2012, pp. 421–434. URL https://doi.org/10.3397/1.3701021.

[8] James, M. M., Salton, A. R., Downing, J. M., Gee, K. L., Neilsen, T. B., Reichman, B. O., McKinley, R., Wall, A. T., and Gallagher, H., "Acoustic Emissions from F-35 Aircraft during Ground Run-Up," *21st AIAA/CEAS Aeroacoustics Conference*, 2015. URL https://doi.org/10.2514/6.2015-2375.

[9] Tam, C. K., Aubert, A. C., Spyropoulos, J. T., and Powers, R. W., "On the Dominant Noise Components of Tactical Aircraft: Laboratory to Full Scale," *23rd AIAA/CEAS Aeroacoustics Conference*, 2017. URL https://doi.org/10.2514/6.2017-3516.

[10] Leete, K. M., Wall, A. T., Gee, K. L., Neilsen, T. B., James, M. M., and Downing, J. M., "Dependence of High-performance Military Aircraft Noise on Frequency and Engine Power," *2018 AIAA/CEAS Aeroacoustics Conference*, 2018. URL https://doi.org/10.2514/6.2018-2826.

[11] Wall, A. T., Gee, K. L., Neilsen, T. B., McKinley, R. L., and James, M. M., "Military jet noise source imaging using multisource statistically optimized near-field acoustical holography," *The Journal of the Acoustical Society of America*, Vol. 139, 2016, pp. 1938–1950. URL https://doi.org/10.1121/1.4945719.

[12] Harker, B. M., Neilsen, T. B., Gee, K. L., Wall, A. T., and James, M. M., "Spatiotemporal-Correlation Analysis of Jet Noise from a High-Performance Military Aircraft," *AIAA Journal*, Vol. 54, No. 5, 2016, pp. 1554–1566. URL https://doi.org/10.2514/1.J054442.

[13] Ffowcs Williams, J. E., Simson, J., and Virchis, V. J., "'Crackle': An annoying component of jet noise," *Journal of Fluid Mechanics*, Vol. 71, 1975, pp. 251–271. doi:10.1017/S0022112075002558.

[14] Krothapalli, A., Venkatakrishnan, L., and Lourenco, L., *Crackle - A dominant component of supersonic jet mixing noise*, American Institute of Aeronautics and Astronautics, 2000. doi:10.2514/6.2000-2024.

[15] Gee, K. L., Russavage, P. B., Neilsen, T. B., Swift, S. H., and Vaughn, A. B., "Subjective rating of the jet noise crackle percept," *The Journal of the Acoustical Society of America*, Vol. 144, No. 1, 2018, pp. EL40–EL45.

[16] Russavage, P. B., Neilsen, T. B., Gee, K. L., and Swift, S. H., "Rating the perception of jet noise crackle," *Proc. Mtgs. Acoust.*, Vol. 33, 2018, p. 040001. doi:10.1121/2.0000821.

[17] Swift, S. H., Gee, K. L., and Neilsen, T. B., "Testing two crackle criteria using modified jet noise waveforms," *The Journal of the Acoustical Society of America*, Vol. 141, No. 6, 2017, pp. EL549–EL554. doi:10.1121/1.4984819.

[18] Rasband, R. D., Wall, A. T., Gee, K. L., Swift, S. H., Wagner, C. M., Murphy, W. J., and Kardous, C. A., "Impulse noise measurements of M16 rifles at Marine Base Quantico," *Proceedings of Meetings on Acoustics*, Vol. 33, No. 1, 2018, p. 040003. doi:10.1121/2.0001010.

[19] Reichman, B., Harker, B., Stout, T., Whiting, E., Gee, K., and Neilsen, T., "Acoustical measurements during a static firing of the Space Launch System solid rocket motor," *Proceedings of Meetings on Acoustics*, Vol. 25, No. 1, 2015, p. 045006. doi:10.1121/2.0000646.

[20] Reichman, B. O., Harker, B. M., Neilsen, T. B., Gee, K. L., and Ohm, W.-S., "Acoustic measurements in the far field during QM-2 solid rocket motor static firing," *Proceedings of Meetings on Acoustics*, Vol. 29, No. 1, 2016, p. 045008. doi:10.1121/2.0000727.

[21] Taylor, T., Gee, K. L., Giraud, J. H., Sommerfeldt, S. D., Blotter, J. D., and Wiederhold, C. P., "On the use of prepolarized microphone systems in rocket noise measurements," *Proceedings of Meetings on Acoustics*, Vol. 14, No. 1, 2011, p. 040005. doi:10.1121/1.4772736.

[22] Bateman, V., and Merritt, R., "Validation of Pyroshock Data," *Journal of the IEST*, Vol. 55, No. 1, 2012, pp. 40–56. doi:10.17764/jiet.55.1.2q4650xqt7j0k506.

[23] Reichman, B. O., Gee, K. L., Neilsen, T. B., Downing, J. M., James, M. M., Wall, A. T., and McInerny, S. A., "Characterizing acoustic shocks in high-performance jet aircraft flyover noise," *The Journal of the Acoustical Society of America*, Vol. 143, 2018. doi:10.1121/1.5026026.

[24] Gee, K. L., Neilsen, T. B., Wall, A. T., Downing, J. M., James, M. M., and McKinley, R. L., "Propagation of crackle-containing jet noise from high-performance engines," *Noise Control Engineering Journal*, Vol. 64, 2015, pp. 1–12.

[25] Wall, A. T., Gee, K. L., Neilsen, T. B., McInerny, S. A., and James, M. M., "Investigation of multi-lobed fighter jet noise sources using acoustical holography and partial field decomposition methods," *21st AIAA/CEAS Aeroacoustics Conference*, 2015. URL https://doi.org/10.2514/6.2015-2379.

[26] Reichman, B. O., Wall, A. T., Gee, K. L., Neilsen, T. B., Downing, J. M., James, M. M., and McKinley, R., "Modeling far-field acoustical nonlinearity from F-35 aircraft during ground run-up," *54th AIAA Aerospace Sciences Meeting*, 2016, p. 1888.